AIP Advances

The statistics of the Debye–Hückel limiting law

Cite as: AIP Advances **12**, 115001 (2022); https://doi.org/10.1063/5.0122869
Submitted: 26 August 2022 • Accepted: 02 October 2022 • Published Online: 01 November 2022

Lodin Ellingsen and Tore Haug–Warberg

The statistics of the Debye–Hückel limiting law

Cite as: AIP Advances 12, 115001 (2022); doi: 10.1063/5.0122869
Submitted: 26 August 2022 • Accepted: 2 October 2022 •
Published Online: 1 November 2022

Lodin Ellingsen[a] and Tore Haug-Warberg[b]

AFFILIATIONS

Department of Chemical Engineering, Norwegian University of Science and Technology, NO-7491 Trondheim, Norway

[a]Electronic mail: lodin.ellingsen@ntnu.no
[b]Author to whom correspondence should be addressed: tore.haug-warberg@ntnu.no

ABSTRACT

The Debye–Hückel Limiting Law (DHLL) correctly predicts the thermodynamic behavior of dilute electrolyte solutions. Most articles and books explain this law using Peter Debye and Erich Hückel's original formalism of linearizing the Poisson–Boltzmann equation for a simple electrolyte model. Brilliant in its own right, this approach does not fully explain which microstates contribute in the range of the Debye–Hückel theory. Notably, the original formalism does not establish the Energy Multiplicity Distribution (EMD), which is the energy distribution of a system's microstates. This work establishes an analytical expression for the EMD that satisfies the DHLL. Specifically, an EMD that is proportional to $\exp(aU_{\mathrm{el}}^3)$ satisfies the DHLL for a monovalent electrolyte solution. Here, U_{el} is the effective electrostatic energy due to ion–ion interactions. The proposed proportionality shows quantitative agreement with the simulated EMDs of a Coulomb lattice gas that corresponds to an aqueous sodium chloride solution at a concentration of 3.559×10^{-4} M. The lattice gas that is used does not incorporate solvent molecules, but the Coulomb interactions are scaled through a permittivity that emulates the solvent—similar to the Debye–Hückel theory. Moreover, this work explains the proportionality by partitioning U_{el} into a set of energy contributions using minimal spanning graphs. This discussion on the EMD is new in the field. It widens the scope of the Debye–Hückel theory and could lead to a new parameterization option for developing equations of state.

NOMENCLATURE

CLG	Coulomb Lattice Gas
DH	Debye–Hückel
DHLL	Debye–Hückel Limiting Law
EMD	Energy Multiplicity Distribution
MC	Monte Carlo

I. INTRODUCTION

In less than a year, it will be 100 years since Peter Debye and Erich Hückel presented their seminal paper[1] on the thermodynamics of electrolyte solutions. Their approach, known as the Debye–Hückel (DH) theory, correctly predicts the behavior of sufficiently dilute electrolyte solutions. Since then, this theory has become the standard approach to introducing the thermodynamics of charged systems. Whether the field is plasma physics,[2] electrochemistry,[3] or electrolyte equations of state,[4] it is likely that the DH theory is the benchmark approach for modeling the long-range interactions between charged molecules. Old but still valid, the gracefully simple DH theory is far from obvious and leaves many confused by its subtle approximations and abstract electrolyte solution model.

The standard derivation of the DH theory follows three distinct steps:[1,4–6]

1. Introducing an electrolyte model where a central ion (species i) is a sphere of radius a_i with a point charge q_i at the center. An ion does not interact with other discrete ions but rather with the surrounding charge density called the ionic-atmosphere. All other interactions are modeled by restricting ions to be separated farther apart than the ion radius. The charge distribution of the ionic-atmosphere corresponds to the time-average positions of the surrounding ions. The contribution of the solvent scales the Coulomb interaction between the central ion and its ionic-atmosphere, as a dielectric continuum.
2. Deriving the contribution of the ionic-atmosphere to the internal per-ion energy. It is assumed that the charge distribution of the ionic-atmosphere follows a Boltzmann

distribution. After linearizing the Boltzmann distribution, the spherical Poisson–Boltzmann equation leads to an expression of the electrostatic energy felt by the central ion due to the surrounding ionic-atmosphere. By summing over the contribution from all ions, the resulting DH model for the total electrostatic energy U_{el} is

$$U^{\mathrm{DH}}(N_i, V, T) = -\sum_{i=1}^{s} \frac{N_i z_i^2 q^2}{8\pi\varepsilon_{\mathrm{s}}} \frac{\kappa}{1+\kappa a_i}. \tag{1}$$

N_i and z_i are the number of ions and the unit charge of ionic species i, whereas V, T, ε_{s}, q, s, and k_{B} are the volume, temperature, permittivity of the solvent, elementary charge, number of different ionic species, and Boltzmann constant, respectively. The Debye length $1/\kappa$, defined as

$$\kappa^2 \triangleq \frac{q^2}{\varepsilon_{\mathrm{s}} k_{\mathrm{B}} T V} \sum_{i=1}^{s} N_i z_i^2, \tag{2}$$

is the characteristic length for the effective Coulomb interaction between ions in an electrolyte solution.

3. Estimating the Helmholtz energy and mean-ionic activity coefficient expressions that correspond to Eq. (1). The partial charging process[4,5,7–9] is now the standard method for obtaining the Helmholtz energy. The Helmholtz energy is then equal to the work required to charge each ion in the presence of the ionic-atmosphere at constant composition, temperature, volume, and permittivity of the solvent. For a binary salt with ions of identical radii a, the logarithm of the mean-ionic activity coefficient calculated from the resulting Helmholtz energy expression is

$$\ln\left(\gamma_{\pm}^{\mathrm{DH}}\right) = -\frac{q^2|z_+ z_-|}{8\pi\varepsilon_{\mathrm{s}} k_{\mathrm{B}} T} \frac{\kappa}{1+\kappa a}. \tag{3}$$

The subscripts + and − denote the cation and anion, respectively. Linearizing Eq. (3) while neglecting higher-order terms leads to the Debye–Hückel Limiting Law (DHLL),

$$\ln\left(\gamma_{\pm}^{\mathrm{DHLL}}\right) = -\frac{q^2|z_+ z_-|}{8\pi\varepsilon_{\mathrm{s}} k_{\mathrm{B}} T}\kappa. \tag{4}$$

Remarkably, the DHLL captures the universal thermodynamic behavior for sufficiently dilute electrolyte solutions.[10–12] The corresponding limiting expression for the total electrostatic energy, found by linearizing Eq. (1) at $\kappa = 0$, is

$$U^{\mathrm{DHLL}}(N_{\mathrm{ions}}, V, T) = -\frac{N_{\mathrm{ions}} q^2|z_+ z_-|}{8\pi\varepsilon_{\mathrm{s}}}\kappa. \tag{5}$$

Here N_{ions} is the total number of cations and anions. Equations (4) and (5) show that the limiting expressions for the mean-ionic activity coefficient and electrostatic energy satisfy $U^{\mathrm{DHLL}} = N_{\mathrm{ions}} k_{\mathrm{B}} T \ln\left(\gamma_{\pm}^{\mathrm{DHLL}}\right)$.

The theory outlined above is conceptually simple but not trivial and is still an active research area. In their 2018 review, Kontogeorgis *et al.*[13] summarized how the DH theory should be used in equations of state. Their study lists 17 unresolved questions regarding the current understanding of the DH theory and electrolyte thermodynamics. The questions concern the effects of modeling solvation effects through the so-called Born term (not relevant for this work), whether the complete DH theory or the DHLL should be used in modeling, and under which conditions the DH theory is valid. In recent years, there have been several attempts at resolving the challenges of the DH and related theories. Simonin[14] argued that the Born term, which corrects the DH theory by considering the changes in the permittivity of a solution with composition, does not accurately model the ion–solvent effects of electrolyte solutions. Shilov and Lyashchenko[15] and subsequent papers[8,16–21] developed a thermodynamically consistent DH-based theory that considers the change in permittivity due to the presence of ions during the partial charging process. Sun *et al.*[19] analyzed how to parameterize the ion radius and static permittivity in the DH theory. In a series of corrections, several authors argued whether an apparent negative deviation from the DHLL at dilute (and finite) concentrations of highly charged polyvalent ions is physical.[22–25] The aforementioned articles show that there is still a reason to challenge the DH theory and its interpretation.

The thermodynamics of a macroscopic system is governed by the Energy Multiplicity Distribution (EMD) of the system's microstates. One early study on characterizing the microstates of electrolyte solutions was conducted by Milner[26,27] in 1912 and 1913. He attempted to establish the limiting behavior of dilute electrolyte solutions by estimating the number of microstates (and their energies) for a small Coulomb gas system. Debye and Hückel considered Milner's work inconclusive in their 1923 article. In a spirit similar to Milner's approach, this article seeks to establish an expression for the energy distribution of a system's microstates—the Energy Multiplicity Distribution (EMD)—that corresponds to the limiting thermodynamics of dilute electrolyte solutions. The EMD is characterized by

1. the number of microstates with an energy E for systems with discrete energies and
2. the number of microstates whose energies lie in the range from E to $E + \mathrm{d}E$ for systems with continuous energies.

For a canonical ensemble with $\beta \triangleq 1/(k_{\mathrm{B}} T)$, n_m microstates and n_e possible energies, the EMD [denoted by $g(E)$] contains all thermodynamic information through the canonical partition function

$$\mathcal{Z} \triangleq \sum_{i=1}^{n_m} e^{-\beta E_i} = \sum_{j=1}^{n_e} g(E_j) e^{-\beta E_j}. \tag{6}$$

This article reveals the distribution of microstates that govern the universal thermodynamic behavior of monovalent dilute electrolyte solutions by

1. developing an expression for the EMD satisfying the DHLL,
2. verifying the EMD expression by simulating a simple lattice electrolyte solution model, and
3. partitioning the simulated EMD into a set of minimal spanning graphs (defined in Sec. IV).

The physics of dilute electrolyte solutions presented here is from a different but complementary approach to the standard DH theory.

II. EMD OF A DILUTE ELECTROLYTE SOLUTION

This section derives the functional form of an EMD such that it recovers the DHLL for monovalent electrolyte solutions in the thermodynamic limit of $n_m \to \infty$.

In the thermodynamic limit, macroscopic observables take on deterministic values. Accordingly, the most probable per-entity energy $\tilde{E}/N$ for a system with N molecular entities[28] and a given β must converge to the expected per-entity energy $\langle E\rangle/N$ for large systems (a rigorous proof requires Gibbs measures[29]). Here,

$$\tilde{E} \triangleq \underset{E_i \in E_1,\ldots,E_{n_e}}{\arg\max}\, g(E_i)e^{-\beta E_i} \tag{7}$$

and

$$\langle E\rangle \triangleq \frac{1}{\mathcal{Z}}\sum_{i=1}^{n_e} E_i g(E_i)e^{-\beta E_i} \tag{8}$$

in the canonical ensemble. Similarly, the most probable per-ion electrostatic energy due to ion–ion interactions must converge to that predicted by Eq. (5) for increasingly dilute electrolyte solutions.

The expected and most probable energies for macroscopic monovalent electrolyte solutions that follow the DHLL satisfy

$$U^{\mathrm{DHLL}} = -C\frac{\beta^{1/2}N_{\mathrm{ions}}^{3/2}}{V^{1/2}}, \tag{9}$$

where $C \triangleq (8\pi)^{-1}q^3\varepsilon_s^{-3/2}$. From the ansatz that the EMD of an electrolyte solution is of the form

$$g(U_{\mathrm{el}}; N_{\mathrm{ions}}, V) = be^{-a(N_{\mathrm{ions}},V)|U_{\mathrm{el}}|^k}, \tag{10}$$

the most probable energy is

$$\tilde{U}_{\mathrm{el}} = -\left(\frac{\beta}{a(N_{\mathrm{ions}},V)(k-1)}\right)^{\frac{1}{k-1}}. \tag{11}$$

Here, a is a function that depends on N_{ions} and V, b is a constant, and k is a real number. In Eq. (11), $\tilde{U}_{\mathrm{el}}$ is the stationary point of $g(U_{\mathrm{el}})\exp(-\beta U_{\mathrm{el}})$ found by setting the derivative

$$\frac{\mathrm{d}\,\ln\left(g(U_{\mathrm{el}})e^{-\beta U_{\mathrm{el}}}\right)}{\mathrm{d}(-U_{\mathrm{el}})} = -a(N_{\mathrm{ions}},V)(k-1)(-U_{\mathrm{el}})^{k-1} + \beta \tag{12}$$

to zero and solving for U_{el}. The exponent k must be equal to 3 for Eq. (11) to recover the $\beta^{\frac{1}{2}}$ proportionality from Eq. (9). Substituting $k = 3$ into Eq. (11) and comparing with Eq. (9) give

$$a(N_{\mathrm{ions}},V) = \frac{V}{2C^2N_{\mathrm{ions}}^3}. \tag{13}$$

The final expression for an EMD whose most probable energy corresponds to the DHLL for a monovalent electrolyte solution is

$$g(U_{\mathrm{el}}; N_{\mathrm{ions}}, V) = be^{\frac{V}{2C^2N_{\mathrm{ions}}^3}U_{\mathrm{el}}{}^3}. \tag{14}$$

As previously discussed, macroscopic observables converge to those of the most probable state in the thermodynamic limit. Hence, a sufficiently large system satisfies the DHLL if it has an EMD of the analytical form of Eq. (14). Note that

1. Equation (14) only applies for $U_{\mathrm{el}} < 0$ as the DHLL only predicts negative energies. Hence, $|U_{\mathrm{el}}|^3 = -U_{\mathrm{el}}^3$, which makes Eq. (14) consistent with Eq. (10).
2. The functional form in Eq. (10) is not unique, in which there are potentially many other functional forms that could satisfy the DHLL in the limit of infinite dilution.

Appendix A derives an expression that corresponds to the DHLL for a system with an EMD that satisfies Eq. (10) but with a k exponent different from 3.

III. MOLECULAR SIMULATIONS

This work uses Monte Carlo (MC) simulations of a Coulomb lattice gas in combination with weighted linear regression to verify that the EMDs of dilute monovalent electrolyte solutions converge to Eq. (14). Section III A describes the lattice gas, and Sec. III B introduces the MC simulations and the regression method.

A. Coulomb lattice gas

The EMD is estimated for a Coulomb Lattice Gas[30–33] (CLG) that corresponds to an aqueous sodium chloride solution. The model describes N_{ions} fully dissociated cations and anions distributed on a cubic lattice grid where the sites are a distance σ apart. All simulations use the minimum image convention,[34] where each particle only interacts with the closest periodic image of the other ions in the system. Ions interact only according to the Coulomb potential such that the total electrostatic energy between ions (in reduced units) becomes

$$U_{\mathrm{el}}^* = \sum_{i=1}^{N_{\mathrm{ions}}}\sum_{j>i}^{N_{\mathrm{ions}}}\frac{z_iz_j}{r_{ij}^*}. \tag{15}$$

Here, r_{ij} is the distance between ions i and j with charges q_i and q_j. Furthermore, the short-range repulsive forces are modeled indirectly by only allowing one single ion on each lattice site in a given microstate. Table I summarizes the reduced units used in this work.

The distance between two adjacent lattice sites, denoted by σ, is also the closest distance of approach of two ions. In the DH theory,

TABLE I. A summary of the reduced variables used in this work and their definitions.

Property	Symbol	Reduced symbol	Definition
Distance	r	r^*	r/σ
Volume	V	V^*	V/σ^3
Number density	ρ	ρ^*	$\rho\sigma^3$
Charge	q_i	z_i	q_i/q
Energy	E	E^*	$4\pi\varepsilon_s\sigma E/q^2$
Temperature	T	T^*	$4\pi\varepsilon_s\sigma k_B T/q^2$
Thermodynamic beta	β	β^*	$q^2\beta/(4\pi\varepsilon_s\sigma)$

this distance corresponds to the radius a in Eqs. (1) and (3). Ribeiro *et al.*[35] compared different methods for estimating this radius for different aqueous solutions. Their estimate ranges between 2.4×10^{-10} and 7.7×10^{-10} m for sodium chloride in water. This work uses a moderate value of

$$\sigma = 3.6 \times 10^{-10} \text{ m} \tag{16}$$

when simulation results are converted from reduced units to those of the real solution. This value also corresponds to the average of Kielland's[36] estimates for the rounded effective radii of hydrated sodium and chloride ions. All other physical constants and quantities used in this work come from the CRC Handbook of Chemistry and Physics,[37] with the exception of the permittivity of water at 25 °C, which is taken from the study by Malmberg and Maryott.[38]

An in-house program designed explicitly for the CLG has been used for all simulations. This program has been verified to reproduce the radial distributions functions of the study by Sørensen.[11] The CLG leads to much shorter simulation times than its continuous counterpart (the restricted primitive model[39]) because the Coulomb energies between the different lattice sites can be precalculated and tabulated. Since a lattice grid affects the behavior of ions that are close together, a CLG should only be used to investigate phenomena with length scales much longer than the grid spacing. Furthermore, using a CLG without an explicit solvent presumes that it is the long-ranged interactions between ions, not the solvent effects, that dictate whether the EMD of a dilute electrolyte solution has the functional form of Eq. (14).

B. Monte Carlo algorithms

This section explains how naive and Metropolis MC sampling are used to estimate the EMD of the CLG from Sec. III A. All simulated EMDs are approximated by continuous distributions, even though the CLG has discrete energies. Metropolis MC is used for all simulations except when $\beta = 0$ where naive MC sampling is used. At least 1000 samples are discarded at the start of all MC simulations to reduce initialization bias. The section concludes by introducing a weighted least squares procedure for estimating the functional form of simulated EMDs. Table II summarizes all the MC simulations performed in this work.

Naive Sampling: Naive MC sampling[40,41] consists of the following steps:

1. Generate a random and independent microstate.
2. Calculate and record the total energy.
3. Repeat steps 1 and 2 for a large number of microstates.
4. Count the number of microstates with energies within predefined intervals (bins) using a histogram.

A forward Fisher–Yates shuffling algorithm[42,43] in conjunction with Eq. (15) is used to calculate the energy for each microstate. Dividing the number of samples in each histogram bin by the width of the bin leads to a scaled EMD $g_0^s(E)$, where the integrated area is equal to the number of sampled states.[44,45] This $g_0^s(E)$ approximates the real EMD scaled by an unknown value

$$g(E) \propto g_0^s(E). \tag{17}$$

Unfortunately, for large systems, the naive MC simulation only captures the distribution of states close to the most probable energy. A naive MC simulation of a CLG with 100 ions and 10^6 sites will never adequately sample the approximately $(10^6)^{100} = 10^{600}$ microstates. The so-called importance sampling techniques such as Metropolis MC are necessary for sampling the distribution of microstates with less prevalent energies.

TABLE II. Summary of the simulated electrolyte solutions. Column c (M) denotes the corresponding aqueous sodium chloride concentration, and column N_s denotes the number of sampled microstates in an MC simulation. The footnotes present the β^* values (defined in Table I) at which each system is simulated. For reference, 25 °C corresponds to $\beta^* = 1.988$ for the sodium chloride solution.

System	ρ^*	N_{ions}	L^*	c (M)	N_s
A[a]	1.000×10^{-5}	10 000	1000	3.559×10^{-4}	10^4
B[b]	1.001×10^{-4}	10 000	464	3.563×10^{-3}	10^4
C[c]	9.923×10^{-4}	10 000	216	3.532×10^{-2}	10^4
D[a]	1.001×10^{-5}	1000	464	3.563×10^{-4}	10^5
E[a]	9.923×10^{-5}	1000	216	3.532×10^{-3}	10^5
F[a]	1.000×10^{-3}	1000	100	3.559×10^{-2}	10^5
G[a]	9.923×10^{-6}	100	216	3.532×10^{-4}	10^6
H[a]	1.000×10^{-4}	100	100	3.559×10^{-3}	10^6
I[a]	1.027×10^{-3}	100	46	3.657×10^{-2}	10^6
J[d]	7.324×10^{-3}	30	16	2.607×10^{-1}	10^6

[a]Simulated at $\beta^* = -0.2, -0.1, 0.0, 0.3, 0.8, 1.5$, and 2.8.
[b]Simulated at $\beta^* = -0.1, 0.0, 0.3, 0.8, 1.5$, and 2.8.
[c]Simulated at $\beta^* = 0.0, 0.3, 0.8, 1.5$, and 2.8.
[d]Simulated at $\beta^* = 0.0$.

Metropolis Sampling: In Metropolis MC,[40,41,46–48] microstates are sampled differently based on the temperature. For a Metropolis MC simulation with sufficiently many sampled microstates, the probability of sampling a microstate i with energy E_i is proportional to $e^{-\beta E_i}$. Just as for the naive approach, it is possible to approximate a continuous distribution $h_\beta(E)$ of simulated energies using histograms. This distribution satisfies

$$h_\beta(E) \propto g(E)e^{-\beta E}. \tag{18}$$

Substituting the scaled EMD

$$g_\beta^s(E) \triangleq h_\beta(E)e^{\beta E} \tag{19}$$

into Eq. (18) leads to the proportionality $g(E) \propto g_\beta^s(E)$. As for the naive approach, a scaled EMD calculated from a Metropolis MC simulation captures only a limited energy range. Multiple simulations at different temperatures are therefore necessary when investigating a larger section of a system's EMD. A positive simulation temperature accentuates the underlying EMD at negative energies, whereas a physically unrealistic negative temperature accentuates the EMD at positive energies. A system simulated at m different temperatures leads to a set of scaled EMDs denoted by $g_{\beta_1}^s(E), g_{\beta_2}^s(E), \ldots, g_{\beta_m}^s(E)$. These distributions are proportional to the EMD of the system but have different proportionality constants. These constants are not known at the outset, and they must therefore be estimated afterward.

Weighted Least Squares: It will be demonstrated in Sec. V that the EMD of system A (defined in Table II) satisfies $g(U_{\text{el}}) = b \exp\left(-a|U_{\text{el}}|^{2.95}\right)$ for negative energies. Figure 1(a) shows three of

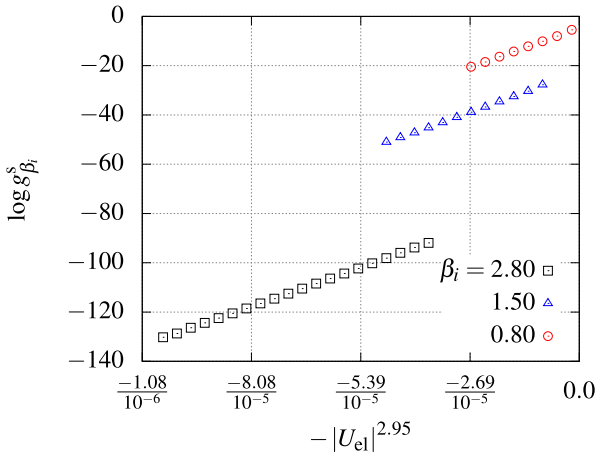

(a) Scaled EMDs (calculated using equation (19)) from MC simulations performed at different temperatures

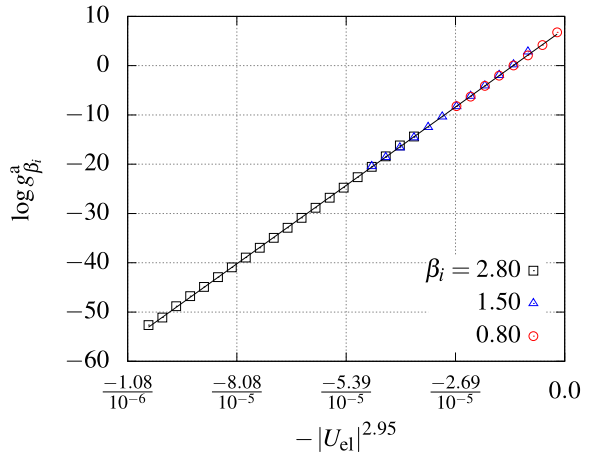

(b) Shifted EMDs with good fit and a small weighted sum of squares

FIG. 1. Scaled (a) and shifted (b) EMDs for three of the simulations of system A performed at different temperatures. The EMD of system A satisfies $g(U_{el}) = b\exp(a|U_{el}|^{2.95})$. The logarithms of the scaled EMDs are shifted to fit a single line using weighted least squares. Figure b is a subset of Fig. 3 from the Results and Discussion section.

the scaled EMDs of this system simulated at different temperatures. When $k = 2.95$, these scaled EMDs satisfy

$$\log g^{s}_{\beta_i}\left(U^{k}_{el}\right) = a|U_{el}|^{k} + b^{(\beta_i)} \tag{20}$$

for the same a but different $b^{(\beta_i)}$ values (since they are scaled differently). Weighted least squares[49,50] leads to the a parameter and $b^{(\beta_i)}$ parameters that best fit the simulated EMDs for a given k by minimizing the weighted sum of squares. The optimal k which minimizes the weighted sum of squares, indicates the functional form from Eq. (10) that best fits the simulated and scaled EMDs. The logarithm of the EMD is then translated in the y direction using the optimized $b^{(\beta)}$ parameters. These shifted EMDs are denoted by $g^{a}_{\beta_i}$ and differ from $g^{s}_{\beta_i}$ and g only by a proportionality factor. Figure 1(b) shows the shifted EMDs for the previous example.

The weighted least squares procedure used in this work is described in Appendix B. Notably, the approach consists of estimating a weighted sum of squares for both the positive and negative branches of the EMD that are denoted by θ_p and θ_n. k_p and k_n that minimize θ_p and θ_n are the k exponents in Eq. (10) that best fit the EMD at positive and negative energies. Optimization of k_p and k_n is one approach to characterize EMDs. Other possibilities can be thought of, but have not been worked out.

IV. MINIMAL SPANNING GRAPHS

The ion interactions that represent a particular microstate can be partitioned into a set of edge-disjoint graphs. The subsequent discussion explains the qualitative behavior of the simulated EMDs, including the asymmetry between the number of states with positive and negative energies, using a set of minimal spanning graphs.

A microstate can be encoded as a complete graph[51] $G = (V, A)$ with vertices $v_i \in V$ and edges $(v_i, v_j) \in A$. In this context, a vertex represents the position (and the charge) of an ion. An edge (v_i, v_j) connects vertices v_i and v_j. The weight of the edge (v_i, v_j) is chosen to be equal to the Euclidean distance between ions i and j and is denoted by $r(v_i, v_j)$. For illustration, Fig. 2(a) shows a complete graph representation of a microstate with five ions.

The concept of a minimum spanning tree[52] is that of an acyclic graph that connects all vertices of the complete graph such that the total edge weight

$$\sum_{(v_i,v_j)\in A_1} r(v_i, v_j) \tag{21}$$

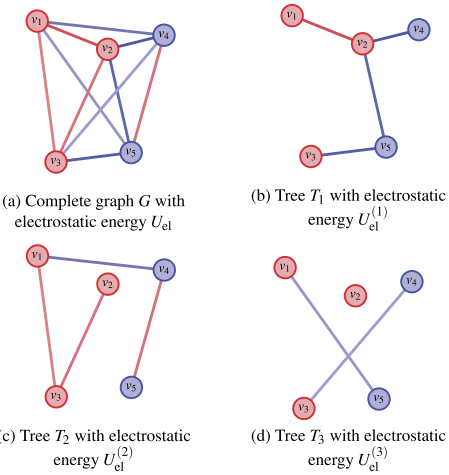

(a) Complete graph G with electrostatic energy U_{el}

(b) Tree T_1 with electrostatic energy $U^{(1)}_{el}$

(c) Tree T_2 with electrostatic energy $U^{(2)}_{el}$

(d) Tree T_3 with electrostatic energy $U^{(3)}_{el}$

FIG. 2. (a)–(d) Illustration of how the pairwise interactions in a microstate with two anions (in blue) and three cations (in red) correspond to a single complete graph or multiple T_1, T_2, and T_3 graphs. Each ion is represented by a vertex v_i, and the edge weight is equal to the separation $r(v_i, v_j)$ between vertices (ions) i and j. The red and blue lines denote positive and negative Coulomb interactions, respectively.

is minimized. The minimum spanning tree $T_1 = (V, A_1)$ hence connects all vertices (ions) in a microstate, with a subset of edges (pairwise interactions) $A_1 \subset A$. Kruskal's algorithm[52] is used to find minimal spanning graphs. The algorithm is greedy, and $r_1 < r_2$ implies $1/r_1 > 1/r_2$, which means that T_1 also corresponds to the tree that connects all ions and maximizes the sum

$$\sum_{(\nu_i,\nu_j)\in A_1} \frac{1}{r(\nu_i,\nu_j)}. \tag{22}$$

Figure 2(b) shows the minimum spanning tree T_1 that connects all five ions mentioned earlier. There is no restriction on which edges are allowed in T_1.

In general, $T_k = (V, A_k)$ is a minimal spanning graph that connects the vertices, excluding all edges in $A_1, \ldots, A_{k-1}$, such that the subtotal edge weight is minimized. T_k can be one single tree or multiple disconnected trees, depending on the edges in the previous graphs. For a CLG, it is likely that T_k is a tree when $k \ll N_{\text{ions}}$, due to the large number of possible edges connecting the ions. The energy of T_k is

$$U_{\text{el}}^{(k)} = \frac{1}{4\pi\varepsilon_s} \sum_{(\nu_i,\nu_j)\in A_k} \frac{q_i q_j}{r(\nu_i,\nu_j)}. \tag{23}$$

A complete graph can be partitioned into $n_{\max} \in \{\lfloor N_{\text{ions}}/2 \rfloor, \lfloor N_{\text{ions}}/2 + 1 \rfloor, \ldots, N_{\max} - 1\}$ non-empty (a graph with at least one edge) and edge-disjoint minimal spanning graphs. This $n_{\max}$ differs for each microstate in the MC simulation. Summing the energy for the first $n_{\max}$ graphs recovers Eq. (15),

$$U_{\text{el}} = U_{\text{el}}^{(1)} + U_{\text{el}}^{(2)} + \cdots + U_{\text{el}}^{(n_{\max})}. \tag{24}$$

Equation (24) is a kind of series expansion of graphs that partition the interaction of a CLG into increasingly unimportant contributions. Figures 2(b)–2(d) show by example how a microstate of five ions can be partitioned into two minimal spanning edge-disjoint trees and one edge-disjoint graph called T_1, T_2, and T_3.

V. RESULTS AND DISCUSSION

The main finding of this article is that the EMD of a dilute monovalent electrolyte solutions satisfies the proportionality $g(U_{\text{el}}) \propto \exp\left(aU_{\text{el}}^3\right)$. This section verifies this claim for a simulated CLG and explains the qualitative behavior of electrolyte solutions by partitioning ion–ion interactions into edge-disjoint sets of minimal spanning graphs.

A. EMDs and optimization results

This section presents the simulated EMDs for the CLG from Sec. III A and verifies to which extent they correspond to the functional form derived in Sec. II. The weighted least squares procedure introduced at the end of Sec. III B and thoroughly described in Appendix B is used to shift the EMDs from different runs (with different temperatures) so that they fit a single straight line in an optimal way. The section ends with a short discussion on how the DHLL changes with the functional form of the EMD.

The EMDs in this sections are presented (and calculated) in terms of the variable X defined as

$$X \triangleq \begin{cases} \left(\dfrac{U_{\text{el}}}{N_{\text{ions}}}\right)^3, & \text{if } U_{\text{el}} < \ddot{U}_{\text{el}}, \\ \left(\dfrac{U_{\text{el}} - \ddot{U}_{\text{el}}}{N_{\text{ions}}}\right)^{1.2}, & \text{if } U_{\text{el}} \geq \ddot{U}_{\text{el}}. \end{cases} \tag{25}$$

Here, $\ddot{U}_{\text{el}}$ corresponds to the most probable $g(U_{\text{el}})$ and can be estimated by interpolating $g_0^s(U_{\text{el}})$. The branches of X corresponding to energies larger and smaller than $\ddot{U}$ are denoted by X_{p} and X_{n}, respectively. Defining X in this manner ensures that a simulated $g_\beta^s(X)$ is a monotonically increasing function when $X = X_{\text{n}}$, which is consistent with Eq. (14). Furthermore, the definition of X ensures that X_{p} and X_{n} correspond to strictly positive and negative per-ion energies. Appendix C demonstrates that this behavior is correct in the thermodynamic limit where $\ddot{U}_{\text{el}}/N_{\text{ions}}$ converges to zero.

Simulations of a system with an EMD of the form $g(U_{\text{el}}) = b\exp\left(aU_{\text{el}}^3\right)$ for negative energies satisfy the linear proportionality $\log g^s(X_{\text{n}}) \propto X_{\text{n}}$. Figure 3 shows the shifted EMDs for system A in Table II as a function of X. Visual inspection indicates that the negative branch is close to linearity in X_{n}, implying that the CLG at $\rho^* = 10^{-5}$ (almost) satisfies the DHLL over the simulated temperature range. Plotting the logarithm of the EMD as a function of $(U_{\text{el}}/N_{\text{ions}})^{2.95}$ instead of X_{n} reduces the slight curvature in Fig. 3. Furthermore, the positive branch is close to linearity in X_{p}. The linearity of the positive and negative EMD branches indicates a significant asymmetry between the EMD at positive and negative energies, in which they closely follow the functional form from Eq. (10) for two different k exponents. This asymmetry will be discussed in Sec. V B.

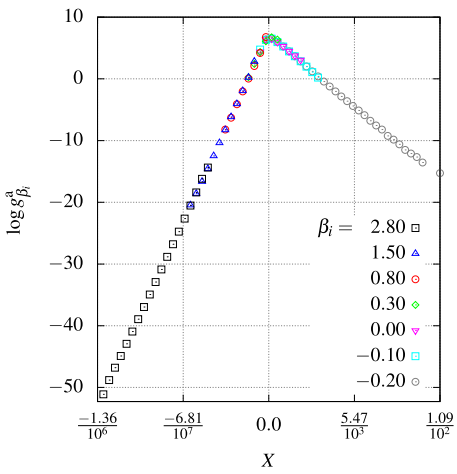

FIG. 3. Shifted EMDs $g_{\beta_i}^a(X)$ for system A. The weighted least squares procedure from Appendix B with optimal $k_{\text{n}} = 2.95$ and $k_{\text{p}} = 1.20$ parameters is used to shift the EMDs. A total of seven β_i (thermodynamic beta) are required to span 60 decades in the diagram.

TABLE III. The expectation value and standard deviation of θ_n for the systems in Table II as a function of k_n. The optimal k_n parameter is written in red.

System	k_n =	2.65	2.70	2.75	2.80	2.85	2.90	2.95	3.00
A		19.06 ± 0.67	13.18 ± 0.32	8.38 ± 0.39	5.31 ± 0.39	3.19 ± 0.36	2.23 ± 0.33	2.21 ± 0.29	2.92 ± 0.28
B		21.80 ± 1.55	13.89 ± 1.43	10.54 ± 0.78	9.90 ± 0.92	11.86 ± 0.56	17.02 ± 0.96	24.36 ± 1.10	34.70 ± 1.17
C		115.52 ± 1.65	76.98 ± 1.96	52.84 ± 2.70	36.03 ± 2.19	29.34 ± 0.96	32.70 ± 1.86	44.37 ± 1.00	62.86 ± 1.19
		2.50	2.55	2.60	2.65	2.75	2.80	2.85	2.90
D		33.09 ± 0.94	31.85 ± 0.70	30.21 ± 0.92	30.05 ± 0.86	30.35 ± 1.35	30.95 ± 2.73	31.62 ± 1.84	32.93 ± 2.09
E		30.64 ± 0.53	26.42 ± 0.40	23.01 ± 0.24	21.12 ± 0.53	19.70 ± 0.46	20.41 ± 0.81	21.56 ± 0.41	23.61 ± 0.82
F		51.98 ± 0.67	38.84 ± 0.22	28.73 ± 0.40	21.66 ± 0.58	13.76 ± 0.19	13.10 ± 0.30	14.65 ± 0.49	17.86 ± 0.49
		1.00	1.20	1.40	1.60	1.80	2.00	2.20	2.40
G		17.07 ± 1.39	23.60 ± 2.51	34.91 ± 3.27	48.60 ± 3.81	63.92 ± 4.33	83.94 ± 4.33	110.37 ± 2.98	136.15 ± 8.26
H		27.31 ± 0.38	22.05 ± 0.45	21.52 ± 0.70	24.74 ± 1.39	33.55 ± 1.84	45.81 ± 2.75	63.80 ± 4.15	86.14 ± 7.20
I		148.40 ± 2.47	111.90 ± 1.38	81.70 ± 0.57	58.37 ± 0.30	42.40 ± 0.30	33.28 ± 0.45	31.66 ± 0.81	36.40 ± 2.03
		2.20	2.30	2.40	2.50	2.70	2.80	2.90	3.00
J		4.31 ± 0.32	3.80 ± 0.41	3.28 ± 0.26	2.93 ± 0.36	2.89 ± 0.59	2.18 ± 0.42	2.61 ± 0.88	2.88 ± 0.48

Section III B and Appendix B describe a weighted least squares method for shifting the simulated EMDs and investigating how closely they follow different functional forms. The optimal k_n and k_p, which minimize θ_n and θ_p, indicate the functional form from Eq. (10) that best fits the X_n and X_p branches of the simulated EMDs. For Eq. (14) to be consistent with the DHLL, the optimal k_n parameter must converge to three for sufficiently dilute ($\rho \to 0$) and thermodynamically large ($\frac{1}{\kappa L} \to 0$) ensembles. Tables III and IV reveal how θ_n and θ_p change with different k_n and k_p parameters for the systems in Table II, respectively. Table III suggests that the optimal k_n parameter decreases from ~2.80–2.95 to 2.65–2.80 and to less than 2.20 when the number of ions is reduced from 10 000 ions to 1000 ions and 100 ions, respectively. Similarly, Table IV suggests that optimal k_p for all simulations are in the range 1.05–1.25. At a given density, the optimal k_n seems to approach 3.0 with increasing system size. This behavior supports the claim that the EMD of dilute electrolyte solutions follows the functional form $b \exp(aU_{el}^3)$. k_n changing with system size indicates significant finite-size effects in our simulations, especially for systems with 1000 ions and less.

The Debye length $1/\kappa$ defined in Eq. (2) is a measure of the range of the effective Coulomb interaction between ions in an electrolyte solution.[11,53,54] Sørensen *et al.*[11,12] demonstrated significant finite-size effects in molecular simulations of dilute electrolyte solutions when $1/\kappa$ is of the same order of magnitude as the length of the simulation box L. The Debye length in reduced units for a sodium chloride solution at 25 °C (or equivalently $\beta^* = 1.988$) is 63.26 for $\rho^* = 10^{-5}$, 20.01 for $\rho^* = 10^{-4}$, and 6.33 for $\rho^* = 10^{-3}$. Since the Debye length is proportional to $\beta^{-\frac{1}{2}}$, there are significant finite-size effects for any EMD simulated at $\beta^* \ll 1$. Since the Debye length and the simulation box lengths scale with density according to $1/\kappa \propto \rho^{-1/2}$ and $L \propto \rho^{-1/3}$, the finite-size effects become more pronounced at lower densities (for a fixed number of ions). Increasing finite-size effects at smaller densities explains why the optimal

TABLE IV. The expectation value and standard deviation of θ_p for the systems in Table II as a function of k_p. The optimal k_p parameter is written in red.

System	k_p =	0.95	1.00	1.05	1.10	1.15	1.20	1.25	1.30
A		14.76 ± 0.58	10.08 ± 0.40	6.22 ± 0.46	3.67 ± 0.42	1.92 ± 0.33	1.16 ± 0.35	1.63 ± 0.57	2.91 ± 0.60
B		12.12 ± 0.92	6.91 ± 0.77	3.67 ± 0.68	2.33 ± 0.46	2.24 ± 0.75	2.90 ± 0.53	6.19 ± 1.44	10.60 ± 2.18
C		0.71 ± 0.13	0.67 ± 0.14	0.68 ± 0.21	0.55 ± 0.13	0.56 ± 0.17	0.76 ± 0.26	0.53 ± 0.33	0.64 ± 0.33
D		7.35 ± 0.45	5.92 ± 0.44	5.25 ± 0.62	5.30 ± 0.34	5.28 ± 0.91	5.55 ± 1.08	6.37 ± 0.90	7.25 ± 1.00
E		8.72 ± 0.49	6.91 ± 0.74	5.35 ± 0.44	5.16 ± 0.62	4.56 ± 0.80	4.37 ± 0.82	4.85 ± 0.73	5.55 ± 0.81
F		18.06 ± 0.40	10.78 ± 0.53	5.60 ± 0.26	4.06 ± 0.78	4.63 ± 1.42	6.27 ± 1.16	12.13 ± 2.41	20.64 ± 3.61
G		19.27 ± 1.48	17.75 ± 1.94	15.82 ± 1.92	15.71 ± 1.83	15.24 ± 2.57	17.72 ± 1.85	20.62 ± 3.45	23.08 ± 3.30
H		13.80 ± 0.49	12.09 ± 0.39	11.65 ± 0.87	11.46 ± 0.81	12.44 ± 1.58	14.46 ± 1.49	16.22 ± 0.95	20.18 ± 1.88
I		10.27 ± 1.15	8.76 ± 0.75	8.17 ± 0.74	8.63 ± 0.72	9.14 ± 1.37	10.72 ± 1.34	13.25 ± 0.83	15.44 ± 1.39
J		4.68 ± 0.29	3.68 ± 0.36	3.24 ± 0.47	3.37 ± 0.49	3.18 ± 0.87	3.22 ± 0.73	4.11 ± 0.57	4.43 ± 1.26

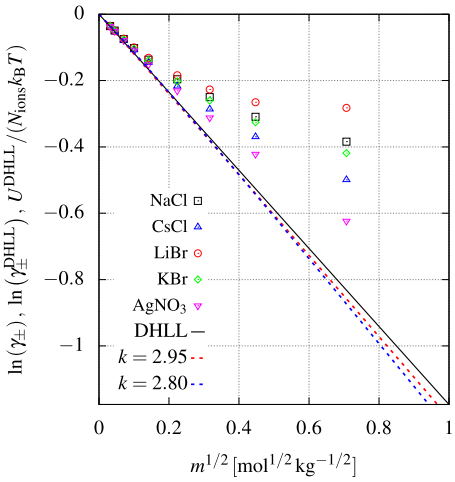

FIG. 4. Comparison of experimental mean-ionic activity coefficients for different monovalent aqueous electrolyte solutions at 25 °C (markers) and different hypothetical limiting laws (lines) as a function of molality. The solid line shows $\ln(\gamma_{\pm}^{\mathrm{DHLL}}) = U^{\mathrm{DHLL}}/(N_{\mathrm{ions}}k_{\mathrm{B}}T)$ according to Eqs. (4) and (5). The dashed lines indicate how $U^{\mathrm{DHLL}}/(N_{\mathrm{ions}}k_{\mathrm{B}}T)$ would change if the EMD of an electrolyte solution followed Eq. (10) with the optimal exponents of systems A and F, equal to $k = 2.95$ and $k = 2.80$, respectively, instead of 3. These dashed lines correspond to Eq. (A6) set equal to the DHLL at the densities of systems A ($\rho^* = 10^{-5}$) and F ($\rho^* = 10^{-3}$).

k_{n} drops under 3.0 at low densities for systems with 1000 ions and less.

Appendix A explains how the DHLL changes with the functional form of the EMD. For instance, Figs. 4 and 5 illustrate how the DHLL would differ if the EMD followed Eq. (10) with a k exponent equal to the optimal exponents of systems A ($k = 2.95$) and F ($k = 2.80$), respectively, instead of 3 in the thermodynamic limit. These hypothetical limiting laws are arbitrarily set equal to the DHLL at the density of systems A ($\rho^* = 10^{-5}$) and F ($\rho^* = 10^{-3}$), respectively. There are insufficient data to establish whether an exponent of $k = 3$ (DHLL) or $k = 2.95$ best fits the limiting behavior of dilute electrolyte solutions, given the limited range of experimental concentrations. On this ground, the EMDs for system A are actually indiscernible from the DHLL when compared with available experimental data.

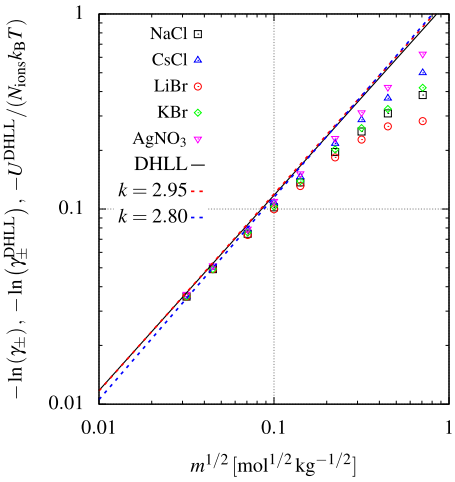

FIG. 5. Figure 4 with logarithmic axes. The limiting law with a computer simulated exponent $k = 2.95$ is barely discernible from the DHLL.

B. The asymmetric EMD of dilute electrolyte solutions

The EMD of dilute electrolyte solutions is asymmetric for positive and negative energies. This behavior is experimentally observed in Fig. 3 (quantified by the difference between the optimal k_{n} and k_{p} parameters in Tables III and IV). To explain the fundamental difference between the EMDs at positive and negative energies, ion–ion interactions can be partitioned into minimal spanning graphs, as explained in Sec. IV. A discussion on what the asymmetry implies about the universal limiting behavior of dilute electrolyte solutions is given at the end of this section.

System J has only 30 ions, but the tables given above still indicate that the system exhibits the same qualitative behavior as the larger ensembles. In Fig. 6, the EMD of this system has been partitioned into a set of minimal spanning graphs. Appendix D demonstrates that the net number of positive Coulomb interactions in a tree T_k follows a Gaussian (and symmetric) distribution about zero for the CLG in the thermodynamic limit. This behavior implies that $g(U_{\mathrm{el}}^{(k)})$ is symmetric as T_k is equally likely to have a certain surplus in the number of negative or positive ion–ion interactions. Accordingly, any asymmetricity for $U^{(1)}$ and $U^{(2)}$ shown in Fig. 6 is due to the simulation box having a finite size. There exists a mathematical proof that the distribution of the sum of two or more symmetric and *independent* random variables must be symmetric.[55] On the other hand, Fig. 6 demonstrates that the energy distribution of $U_{\mathrm{el}}^{(1)} + U_{\mathrm{el}}^{(2)} + \cdots + U_{\mathrm{el}}^{(k)}$ is without doubt asymmetric for $k > 1$. This implies that the energies of the different graphs are correlated.

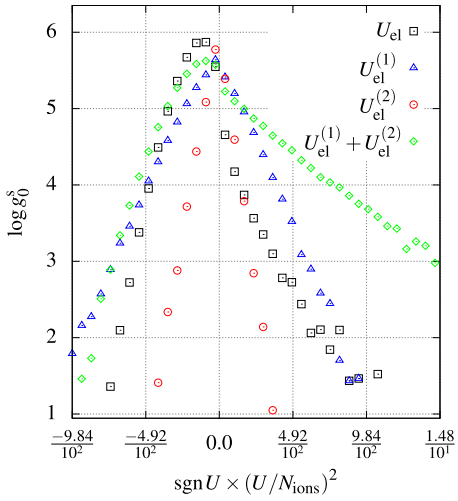

FIG. 6. Scaled EMD for system J partitioned into different minimal spanning graphs. The total electrostatic energy (U_{el}) corresponds to the energy of at least 15 graphs.

The asymmetry in the EMD of system J at positive and negative energies is evident when considering the energy distribution of the first two graphs. Figure 6 demonstrates that the distribution of $U_{\text{el}}^{(1)} + U_{\text{el}}^{(2)}$ is smaller in magnitude than that of $U_{\text{el}}^{(1)}$ for sufficiently negative energies and larger than $U_{\text{el}}^{(1)}$ for sufficiently positive energies. This observation implies that $U_{\text{el}}^{(1)}$ is correlated with a positive $U_{\text{el}}^{(2)}$ for both sufficiently negative and positive energies. A simple one-dimensional system explains why this behavior is expected for systems with clusters of alternating and non-alternating charges.

A one-dimensional Ising model with nearest and next-nearest neighbor interactions[56,57] can be used to explain the nature of the EMDs' asymmetry. The charges are spread equidistantly along a one-dimensional line, where each charge is equally likely to be positive or negative. In this model, the energy contribution from two neighboring charges is either $+\varepsilon$ or $-\varepsilon$. Similarly, the energy contribution from next-nearest neighboring charges is $\pm\frac{3}{4}\varepsilon$. The graphs T_1 and T_2 contain all the nearest and next-nearest neighbor interactions with energies $U^{(1)}$ and $U^{(2)}$, respectively. Figure 7 shows a microstate with five alternating charges and a microstate with five non-alternating charges. The nearest-neighbor energy is $U^{(1)} = -4\varepsilon$ in the alternating microstate and $U^{(1)} = +4\varepsilon$ in the non-alternating microstate. Both microstates have a next-nearest neighbor energy of $U^{(2)} = +\frac{9}{4}\varepsilon$. Notice how in this simple example the alternating and non-alternating sequence of charges lead to a negative or a positive nearest neighbor energy but always to a positive next-nearest neighbor energies. For alternating charges, therefore, the nearest neighbor and next-nearest neighbor interactions are destructive in which they have opposite signs. Oppositely, these energies are always constructive and positive for non-alternating charges. The example in the next paragraph demonstrates that microstates with negative and positive nearest neighbor energies tend to have more alternating and non-alternating charges, respectively.

Consider the previously introduced one-dimensional Ising model with $N_c = 30$ charges. Figure 8 shows the EMD of this system partitioned into $U^{(1)}$, $U^{(2)}$, and $U^{(1)} + U^{(2)}$ contributions. The system exhibits the same qualitative behavior as electrolyte solutions and is small enough where one can calculate all of its 2^{30} microstates. Just as for system J (see Fig. 6), the distribution of $U^{(1)}$ and $U^{(2)}$ is

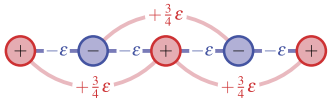

(a) Alternating charges:
$U^{(1)} = -4\varepsilon$ and $U^{(2)} = +\frac{9}{4}\varepsilon$.

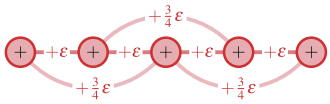

(b) Non-alternating charges:
$U^{(1)} = +4\varepsilon$ and $U^{(2)} = +\frac{9}{4}\varepsilon$.

FIG. 7. (a)–(b) Pairwise interactions in an Ising model with five charges. The nearest neighbor energy $U^{(1)}$ and the next-nearest neighbor energy $U^{(2)}$ correspond to the pairwise interactions in graphs T_1 and T_2.

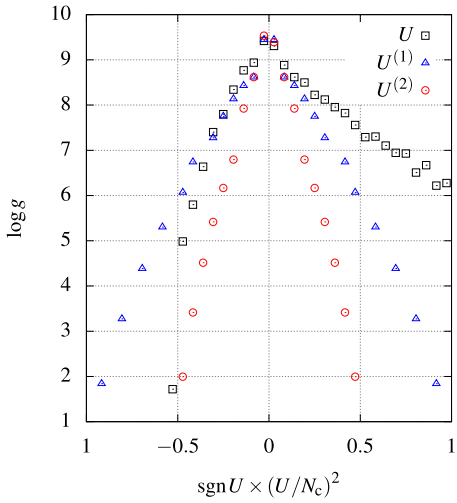

FIG. 8. EMD of the one-dimensional Ising model with 30 charges partitioned into different graphs. The total energy of all minimal spanning graphs satisfies (in this case) $U = U^{(1)} + U^{(2)}$ since the Ising model only considers nearest and next-nearest interactions.

symmetric, and $U^{(1)}$ correlates with a positive $U^{(2)}$ for energies sufficiently large in magnitude. A sequence with three consecutive charges in this system will belong to one of the following triplets:

1. The charges correspond to one of the alternating sequences $+-+$ or $-+-$. Both nearest-neighbor interactions are negative in this triplet, and the next-nearest neighbor interaction is positive.
2. The charges correspond to one of the non-alternating sequences $+++$ or $---$. Both nearest-neighbor and the next-nearest neighbor interactions are positive in such a triplet.
3. The charges satisfy one of the sequences $+--$, $++-$, $-++$, or $--+$. The sum of the nearest neighbor interactions is equal to zero, and the next-nearest neighbor interaction is negative.

The average number of triplets of type x for a microstate with a total nearest-neighbor energy $U^{(1)}$ is denoted by $\langle N_x \rangle_{U^{(1)}}$. Figure 9 illustrates $\langle N_x \rangle_{U^{(1)}}$ for the system with 30 charges. This figure shows that at sufficiently negative and positive $U^{(1)}$, there is a large surplus of alternating triplets $(x = 1)$ and non-alternating triplets $(x = 2)$ with positive next-nearest neighbor energies. This observation implies that although $g(U^{(1)})$ and $g(U^{(2)})$ are symmetric about $U = 0$, $g(U^{(1)} + U^{(2)})$ is asymmetric because all microstates (with sufficiently negative and positive nearest neighbor energies) always have positive next-nearest neighbor energies. Figure 9 also demonstrates that the asymmetry of $U^{(2)}$ at moderately negative and positive energies is primarily due to the triplets of the third type $(x = 3)$ where negative next-nearest neighbor energies dominate.

The one-dimensional Ising model shows that there is an inherent asymmetry in the EMD of electroneutral (satisfied on average in the Ising model) charged systems. Specifically, there is a fundamental difference in how successive $U_{\text{el}}^{(k)}$ energies correlate for a microstate that has alternating vs non-alternating ionic

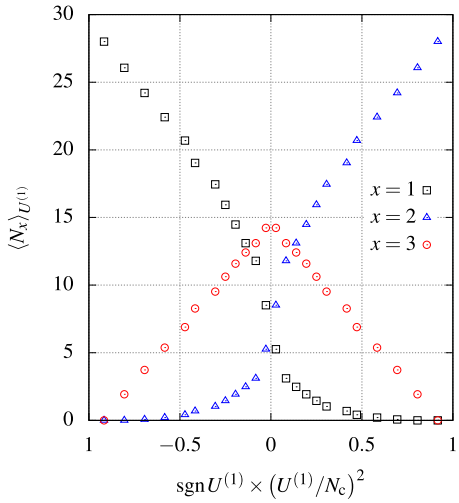

FIG. 9. Average number of triplets of type x in a microstate with a total nearest-neighbor energy $U^{(1)}$ for the one-dimensional Ising model as a function of per-charge energy squared.

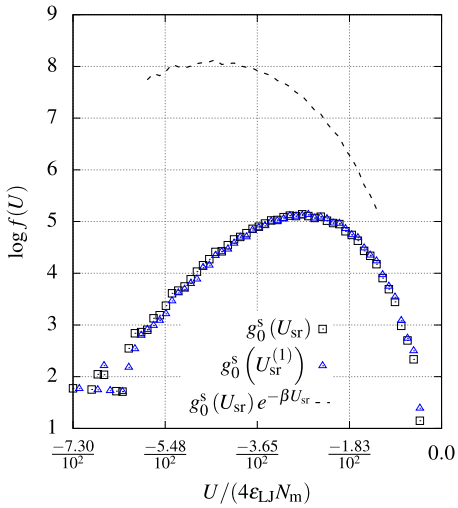

FIG. 10. Scaled EMD for a non-Coulomb lattice gas partitioned into the first minimal spanning graph. This system corresponds to nitrogen gas at (approximately) the density of an ideal gas at 25 °C and 5 bars. The Boltzmann weighted EMD shows the distribution of microstates at a temperature of 600 K. At this temperature and density, the first graph captures almost all significant interactions. The total energy (U_{sr}) has contributions from at least 150 graphs.

charges. The asymmetry in the EMD of electrolyte solutions is because microstates with negative energies are dominated by alternating charges, whereas in microstates with positive energies, the charges are non-alternating. Thus, the $g(U_{el}) = b\,\exp\left(aU_{el}^3\right)$ functional form from Sec. II recovers the statistics of microstates with negative energies. On a side note, the DH theory indirectly predicts that ions alternate in $\mathbb{R}^3$ space as the ionic atmosphere (which reflects the time-averaged positions of all other ions) has an opposite charge to the central ion.

The methodology for simulating EMDs is not limited to CLGs. Appendix E explains how the procedure from Sec. III is used to simulate a non-Coulomb lattice gas corresponding to nitrogen gas at (approximately) the density of an ideal gas at 5 bars and 25 °C. Except for a different pairwise potential and grid spacing, the same algorithm is used to calculate the energies of this lattice gas and CLG. The new set of energies is superscripted sr as in short-range. Figure 10 presents the EMD for such a lattice gas with $N_m = 300$ molecules. This figure also includes the energy distributions for a selection of graphs and the EMD scaled by the Boltzmann factor at 600 K.

Partitioning EMDs into minimal spanning graphs accentuates the differences between the limiting behavior of systems with long-range and short-range interactions. In Fig. 10, the first two graphs T_1 and T_2 almost fully capture the EMD around the most probable Boltzmann weighted energy. Reducing the density further at constant temperature would result in $U_{sr}^{(2)}/U_{sr}^{(1)} \to 0$ such that T_1 alone would capture the complete EMD. There exists an analogy between T_1 and the second virial coefficient B_2 from the virial expansion

$$\frac{pV}{Nk_BT} = 1 + B_2\rho + B_3\rho^2 + \cdots \tag{26}$$

in the low-density limit as both capture all deviations from that of an ideal gas. This is in contrast to electrolyte solutions where multiple graphs $(T_1, T_2, \ldots)$ contribute to the EMD even in the limit $\rho \to 0$. If electrolyte solutions were short-ranged, only T_1 would contribute at the limit of infinite dilution, and $g(U_{el})$ would be symmetric. This disparity between the (number of) minimal spanning graphs for dilute electrolyte solutions and short-ranged systems explains why models (such as the DH theory) are necessary for describing the limiting behavior of electrolyte solutions. Only pairs of molecules sufficiently close together govern the EMD of dilute short-ranged systems, whereas the interactions between a central ion and many of its neighbors dictate the thermodynamics of dilute electrolyte solutions.

The CLG model reproducing the EMD of dilute electrolyte solutions also elucidates the role of the solvent in the DH theory. The model in Sec. III A has no explicit solvent, which demonstrates that an electrolyte solution exhibiting the $\exp\left(aU_{el}^3\right)$ proportionality [which corresponds to the DHLL and $\ln(\gamma_\pm) \propto \kappa$ from Eq. (3)] only depends on ion interactions and is not contingent on ion–solvent effects. The DH theory predicts that using a solvent with a larger permittivity increases the factor a in Eq. (13), which would increase the slope of $\log g^s(X_n)$ in Fig. 3, but beyond this, the exponent $k = 3$ is purely an ion–ion effect.

VI. CONCLUSION

The Debye–Hückel (DH) theory is still, after a century of service, the standard model for calculating the thermodynamic properties of dilute electrolyte solutions. Despite its apparent simplicity, the DH theory conceals several secrets about the universal limiting behavior of dilute electrolyte solutions:

1. What is the prevalence of the underlying microstates?

2. Why do long-range interactions lead to different physics than short-range interactions do for dilute systems?
3. Is the solvent a necessity for observing the Debye–Hückel limiting law (DHLL)?

These are three questions the standard Debye–Hückel theory does not address directly and which we have attempted to explain in this work.

Microstates: The principal claim of this article is that a sufficiently dilute monovalent electrolyte solution exhibits a universal distribution of microstates. Specifically, the energy distribution of the system's microstates (EMD) due to ion–ion interactions satisfies $g(U_{\mathrm{el}}) = b\,\exp\left(aU_{\mathrm{el}}^3\right)$ for some a and b. Molecular simulations of a lattice model have been performed to test the claimed functional form. Notably, this work simulates the EMD of a Coulomb lattice gas (CLG), which approximates an aqueous sodium chloride solution at 25 °C and 3.559×10^{-4} M. The observed EMD spans about 60 decades—made possible by combining Monte Carlo simulations for seven different temperatures. The simulated EMD of a system with 10 000 ions is found to satisfy $g(U_{\mathrm{el}}) = b\,\exp\left(aU_{\mathrm{el}}^{2.95}\right)$. The exponent $k = 2.95$ corresponds to a DHLL where the logarithm of the mean-ionic activity coefficient is proportional to the concentration of salt to the power of $1/2 + 1/234$ instead of the standard $1/2$. The difference is well within the uncertainty of experimental mean-ionic activity coefficients for dilute electrolyte solutions. The optimal k exponent, is observed to approach 3 from below with decreasing ion density, a trend that supports the ansatz on the EMD of dilute electrolyte solutions, which is the basis of this work. Knowing the energy distribution of microstates that corresponds to the limiting behavior of the DH theory sheds light on the thermodynamics of dilute electrolyte solutions from a different angle, which is complementary to the standard derivation.

Short-Range vs Long-Range: The simulated EMDs exhibit an asymmetry for microstates with negative and positive energies. To be specific, the negative and positive branches of the simulated EMDs for systems A–C are approximately proportional to $\exp\left(aU_{\mathrm{el}}^3\right)$ and $\exp\left(-aU_{\mathrm{el}}^{1.2}\right)$, respectively. To investigate the cause of this asymmetry, all pairwise interactions are partitioned into a set of so-called minimal spanning graphs. These graphs are defined such that the energy distribution of each graph is symmetric in the thermodynamic limit. Since simulated EMDs are asymmetric, multiple graphs must contribute to the electrostatic energy of dilute electrolyte solutions. This behavior differs from systems that only have short-range interactions, where a single graph captures all the important interactions in the limit of infinite dilution. The partitioning of the graphs illustrates a fundamental difference between electrolyte solutions and non-Coulomb systems: more interactions are necessary to capture the behavior of increasingly dilute electrolyte solutions compared to fewer ones for increasingly dilute short-ranged systems. In addition, the correlation between the energy of successive graphs shows that microstates with alternating anions and cations in $\mathbb{R}^3$ space dominate for dilute electrolyte solutions.

Solvent: The CLG simulations (closely) reproduce the square root of the concentration proportionality of the DHLL for monovalent electrolytes at a given temperature T without including the solvent as molecules. This observation means that no solvent effects (besides scaling the Coulomb interaction between ions through permittivity ε_s) are necessary to explain the DHLL and the EMD of dilute electrolyte solutions. The CLG and the Debye–Hückel theory both predict that using a solvent with a different permittivity changes the constant a in $\exp\left(aU_{\mathrm{el}}^3\right)$ such that $\varepsilon_s T$ rather than T specifies the thermodynamic state. Investigating the microscopic phenomenon, which leads to this behavior, would further explain the role of the solvent in the Debye–Hückel theory. Increased knowledge could lead to new options for parameterizing equations of state. This, along with deriving the $\exp\left(aU_{\mathrm{el}}^3\right)$ proportionality without relying on the DH theory, is a possible topic of future research on the EMD of dilute electrolyte solutions.

ACKNOWLEDGMENTS

This publication is funded in part by the Research Council of Norway (Grant No. 295007).

AUTHOR DECLARATIONS

Conflict of Interest

The authors have no conflicts to disclose.

Author Contributions

Lodin Ellingsen: Conceptualization (equal); Formal analysis (lead); Investigation (lead); Methodology (lead); Software (lead); Validation (lead); Visualization (lead); Writing – original draft (lead); Writing – review & editing (equal). **Tore Haug-Warberg:** Conceptualization (equal); Formal analysis (supporting); Funding acquisition (lead); Methodology (equal); Project administration (lead); Supervision (lead); Writing – original draft (supporting).Writing – review & editing (equal).

DATA AVAILABILITY

The data that support the findings of this study are available from the corresponding author upon reasonable request.

APPENDIX A: ALTERNATIVE DHLL

This section derives an expression corresponding to the DHLL for a system whose EMD satisfies Eq. (10) but with a k exponent different from 3. It is demonstrated that the DHLL and Eq. (14) scale with volume and charge according to Coulomb's law.

Assume a reference system that consists of N_{pc} point charges in a box of volume V. The magnitude of the point charges is $q_{\pm} \hat{=} |z_i q|$. The EMD of the system when scaled by an arbitrary constant is denoted as $g^{\mathrm{s}}(U_{\mathrm{el}};\ N_{\mathrm{pc}}, V, q_{\pm})$. This quantity is adequately represented by a selection of Ω different microstates. Suppose now there exists a different box with the same number of point charges but with a new volume λV. The scaled EMD of the new system can be calculated from the microstates of the reference system by scaling all distances to fit the new volume. The scaled EMD satisfies

$$g^{\mathrm{s}}(U_{\mathrm{el}};N_{\mathrm{pc}},V,q_{\pm}) = g^{\mathrm{s}}\left(\frac{U_{\mathrm{el}}}{\lambda^{\frac{1}{3}}};N_{\mathrm{pc}},\lambda V,q_{\pm}\right). \tag{A1}$$

Equation (A1) relies on scaling the distances in $\mathbb{R}^3$ with the cube root of volume and calculating the total electrostatic energy of point-charges from Eq. (15). Substituting Eq. (10) into Eq. (A1) gives

$$\frac{a(N_{\mathrm{pc}},\lambda V,q_{\pm})}{a(N_{\mathrm{pc}},V,q_{\pm})} = \lambda^{\frac{k}{3}}, \tag{A2}$$

or equivalently $a \propto V^{\frac{k}{3}}$. A similar argument leads to $a \propto q_{\pm}^{-2k}$. The EMD according to Eq. (10) is

$$g^{\mathrm{s}}(U_{\mathrm{el}};N_{\mathrm{pc}},V) = be^{-a'\frac{V^{\frac{k}{3}}}{q_{\pm}^{2k}}|U_{\mathrm{el}}|^k}, \tag{A3}$$

where $a'(N_{\mathrm{pc}}) \doteq aq_{\pm}^{2k}V^{-\frac{k}{3}}$. The most probable energy becomes

$$\tilde{U}_{\mathrm{el}} = -\left(\frac{\beta q_{\pm}^{2k}}{a'(k-1)V^{\frac{k}{3}}}\right)^{\frac{1}{k-1}}. \tag{A4}$$

For Eq. (A4) to satisfy Euler homogeneity, it can be argued that $a' \propto N_{\mathrm{pc}}^{1-\frac{4k}{3}}$ such that

$$\tilde{U}_{\mathrm{el}} = -\left(\frac{\beta q_{\pm}^{2k}N_{\mathrm{pc}}^{\frac{4k}{3}-1}}{a''(k-1)V^{\frac{k}{3}}}\right)^{\frac{1}{k-1}}, \tag{A5}$$

where $a'' \doteq N_{\mathrm{pc}}^{\frac{4k}{3}-1}a'$. Equations (A3) and (A4) reduce to Eqs. (14) and (9) when $k = 3$, $|z_i| = 1$, and $N_{\mathrm{ions}} = N_{\mathrm{pc}}$.

Equation (A1) assumes that there is a one-to-one correspondence between the microstates before and after scaling the volume of a system. This assumption is not valid for ensembles where ions are restricted by a closest distance of approach, such as the DH theory or the CLG from Sec. III A. For example, decreasing the volume would exclude the microstates where the scaling causes ions to overlap. The previous derivation shows that for a sufficiently dilute electrolyte solution, the EMD (and DHLL) depends on volume and charge as if the energies of a system's microstates scale according to the Coulomb potential for point charges. This observation suggests that the DHLL captures the physics when the predominant contribution to the total electrostatic energy comes from ions far apart that do not overlap when scaling the volume.

Equation (A5) can be conveniently expressed as a function of salt concentration c (or molality m) and a temperature dependent constant D,

$$\frac{U_{\mathrm{el}}}{N_{\mathrm{pc}}} = Dc^{\frac{k}{3(k-1)}}. \tag{A6}$$

Equation (A6) explains how the DHLL differs from that in Eq. (9) when exponent k is allowed to vary.

APPENDIX B: WEIGHTED LEAST SQUARES

Technical details of the weighted least squares procedure used to scale (and shift) EMDs and estimate whether the simulated EMDs are on the functional form of Eqs. (10) and (14). The X_{n} and X_{p} variables used in this section are defined in Eq. (25) and described at the start of Sec. V A.

An EMD that is of the functional form of Eq. (10) satisfies

$$\log g\left(X_{\mathrm{n}}^{\frac{k}{3}}\right) = b_{\mathrm{n}} + a_{\mathrm{n}}|X_{\mathrm{n}}|^{\frac{k}{3}} \tag{B1}$$

in the domain $X = X_{\mathrm{n}}$ for some a_{n} and b_{n} constants.

Weighted least squares can be used to find the optimization parameters $a_{\mathrm{n}}, b_{\mathrm{n}}^{(\beta_1)}, \ldots, b_{\mathrm{n}}^{(\beta_l)}$ that minimize the weighted sum of squares

$$\theta_{\mathrm{n}} = \sum_{k=1}^{l}\sum_{i=1}^{n} w_i^{(\beta_k)}\left|\log g_{\beta_k}^{\mathrm{s}}\left(X_{\mathrm{n},i}^{\frac{k_{\mathrm{n}}}{3}}\right) - \log \hat{g}_{\beta_k}^{\mathrm{s}}\left(X_{\mathrm{n},i}^{\frac{k_{\mathrm{n}}}{3}}\right)\right|^2 \tag{B2}$$

for the estimator

$$\log \hat{g}_{\beta_k}^{\mathrm{s}}\left(X_{\mathrm{n},i}^{\frac{k_{\mathrm{n}}}{3}}\right) = a_{\mathrm{n}}X_{\mathrm{n},i}^{\frac{k_{\mathrm{n}}}{3}} + \sum_{j=1}^{l} b_{\mathrm{n}}^{(\beta_j)}\delta_{kj} \tag{B3}$$

and the set of scaled EMDs $g_{\beta_1}^{\mathrm{s}}(X_{\mathrm{n}}), \ldots, g_{\beta_l}^{\mathrm{s}}(X_{\mathrm{n}})$. In Eqs. (B2) and (B3), k_{n} is a predefined parameter, n is the number of data points per scaled EMD, and δ is the Kronecker delta. The optimal k_{n} parameter, which minimizes the weighted sum of squares, corresponds to the k exponent in Eqs. (10) and (B1) that leads to the best fit of the simulated EMDs. To reduce the effect of outliers, the weights $w_i^{(\beta_k)}$ are set equal to the common logarithm of the number of sampled energies corresponding to a data point $g_{\beta_k}^{\mathrm{s}}(X_{\mathrm{n},i})$.

The same procedure is used to find the optimization parameters $a_{\mathrm{p}}, b_{\mathrm{p}}^{(\beta_1)}, \ldots, b_{\mathrm{p}}^{(\beta_l)}$ that minimize

$$\theta_{\mathrm{p}} = \sum_{k=1}^{l}\sum_{i=1}^{n} w_i^{(\beta_k)}\left|\log g_{\beta_k}^{\mathrm{s}}\left(X_{\mathrm{p},i}^{\frac{k_{\mathrm{p}}}{1.2}}\right) - \log \hat{g}_{\beta_k}^{\mathrm{s}}\left(X_{\mathrm{p},i}^{\frac{k_{\mathrm{p}}}{3}}\right)\right|^2 \tag{B4}$$

for the estimator

$$\log \hat{g}_{\beta_k}^{\mathrm{s}}\left(X_{\mathrm{p},i}^{\frac{k_{\mathrm{p}}}{1.2}}\right) = a_{\mathrm{p}}X_{\mathrm{p},i}^{\frac{k_{\mathrm{p}}}{1.2}} + \sum_{j=1}^{l} b_{\mathrm{p}}^{(\beta_j)}\delta_{kj} \tag{B5}$$

and the scaled EMDs $g_{\beta_1}^{\mathrm{s}}(X_{\mathrm{p}}), \ldots, g_{\beta_l}^{\mathrm{s}}(X_{\mathrm{p}})$.

MC simulations lead to EMDs that are scaled differently depending on the simulation temperature and the number of samples. If the optimization (for a given k_{n} and k_{p}) captures the underlying distribution of states, then the shifted EMD, defined as

$$\log g_{\beta}^{\mathrm{a}}(X) \doteq \begin{cases} \log g_{\beta}^{\mathrm{s}}(X_{\mathrm{n}}) - (b_{\mathrm{m}}^{(\beta)} - b_{\mathrm{m}}^{(0)}), & \text{if } X < 0, \\ \log g_{\beta}^{\mathrm{s}}(X_{\mathrm{p}}) - (b_{\mathrm{p}}^{(\beta)} - b_{\mathrm{p}}^{(0)}), & \text{if } X \geq 0, \end{cases} \tag{B6}$$

can be used to find a common proportionality factor for a set of scaled EMDs $g_{\beta_1}^{\mathrm{s}}(X_{\mathrm{p}}), \ldots, g_{\beta_m}^{\mathrm{s}}(X_{\mathrm{p}})$.

The Results and Discussion section presents the expected value and standard deviation of θ_{n} and θ_{p} for the systems in Table II. These statistical properties are estimated using bootstrapping[58]

with ten bootstrap samples. A single bootstrap sample consists of estimating θ_n and θ_p using weighted least squares for a dataset $g_{\beta_1}^{s,b}(X), \ldots, g_{\beta_l}^{s,b}(X)$ constructed by resampling lN_s of the system's MC simulated energies with replacement.

APPENDIX C: EXPECTED PER-ION ELECTROSTATIC ENERGY

The expected per-ion energy for the EMD of a CLG is zero in the thermodynamic limit. Since macroscopic observables take on deterministic values in a thermodynamic system, it follows that the most *probable* per-ion energy must also go to zero. The most probable electrostatic energy and the expected electrostatic energy follow by inserting $\beta = 0$ into Eqs. (7) and (8).

The expected per-ion electrostatic energy for the CLG from Sec. III A is

$$\begin{aligned}
\mathrm{E}\left[\frac{U_{\mathrm{el}}^*}{N_{\mathrm{ions}}}\right] &\overset{1.}{=} \mathrm{E}\left[\frac{1}{N_{\mathrm{ions}}}\sum_{i=1}^{N_{\mathrm{ions}}}\sum_{j>i}^{N_{\mathrm{ions}}}\frac{z_i z_j}{r_{ij}^*}\right] \\
&\overset{2.}{=} \frac{N_{\mathrm{ions}}-1}{2}\mathrm{E}\left[\frac{z_1 z_2}{r_{12}^*}\right] \\
&\overset{3.}{=} \frac{N_{\mathrm{ions}}-1}{2}\mathrm{E}[z_1 z_2]\mathrm{E}\left[\frac{1}{r_{12}^*}\right] \\
&\overset{4.}{=} -\frac{1}{2}\mathrm{E}\left[\frac{1}{r_{12}^*}\right].
\end{aligned} \tag{C1}$$

The list of equalities is explained below:

1. The total electrostatic energy expression is from Eq. (15).
2. The expectation value for the sum of two random variables X and Y is $E[X+Y] = E[X] + E[Y]$. Here, X and Y do not need to be independent. There are a total of $\frac{N_{\mathrm{ions}}(N_{\mathrm{ions}}-1)}{2}$ pairwise interactions in an ensemble with N_{ions} ions.
3. The expectation value for two independent random variables X and Y is $E[XY] = E[X]\,E[Y]$.
4. There are $2 \times \frac{\frac{N_{\mathrm{ions}}}{2}(\frac{N_{\mathrm{ions}}}{2}-1)}{2} = \frac{N_{\mathrm{ions}}^2}{4} - \frac{N_{\mathrm{ions}}}{2}$ positive (anion–anion and cation–cation) and $\frac{N_{\mathrm{ions}}(N_{\mathrm{ions}}-1)}{2} - 2 \times \frac{\frac{N_{\mathrm{ions}}}{2}(\frac{N_{\mathrm{ions}}}{2}-1)}{2} = \frac{N_{\mathrm{ions}}^2}{4}$ negative (anion–cation) interactions. Accordingly, there is a surplus of $\frac{N_{\mathrm{ions}}}{2}$ negative interactions, that is, $\mathrm{E}[z_1 z_2] = -\frac{\frac{N_{\mathrm{ions}}}{2}}{\frac{N_{\mathrm{ions}}(N_{\mathrm{ions}}-1)}{2}}$.

Since the expected distance between two random points in a box scales linearly with the box length, the expected inverse distance between two non-overlapping ions decreases to zero in the thermodynamic limit. Equation (C1) shows that if $\mathrm{E}[\frac{1}{r_{12}^*}]$ goes to zero, then so does the expected per-particle energy.

APPENDIX D: DISTRIBUTION OF EDGES IN A SINGLE GRAPH

The net number of positive edges in a tree T_k becomes Gaussian about zero in the thermodynamic limit for a monovalent electrolyte solution (the definitions of graphs, trees, edges, and vertices are those of Sec. IV).

Let T_k be a tree connecting N_{ions} monovalent ions that are cations or anions with equal probability. The net number of positive interactions in T_k is

$$S_k = \sum_{(v_i,v_j)\in A_k} z_i z_j. \tag{D1}$$

A procedure for calculating S_k for a given microstate is outlined below:

1. Let $T_k' = (V_k', A_k')$ be a graph where A_k' is an empty set and V' consists of a single random ion modeled as vertex v_1.
2. Pick a random ion $v_j \in V_k \backslash V_k'$ with an edge $(v_j, v_i) \in A_k \backslash A_k'$ such that $v_i \in V'$.
3. Add v_j and (v_j, v_i) to V' and A'.
4. Calculate $z_i z_j$.
5. Repeat steps 2–4 for all $N_{\mathrm{ions}} - 1$ edges until $T_k = T_k'$ and all terms in Eq. (D1) are found.

Ion j is equally likely a cation or anion in steps 2–4, which means there is an equal probability that $z_i z_j$ is +1 or −1. Accordingly, each summation term in Eq. (D1) is equally likely to be minus or plus one. The central limit theorem guarantees that the distribution of a sum of identically distributed and independent variables converges to a Gaussian about their average. This result is not contingent on T_k being a tree, but it is valid if T_k is a graph with sufficiently many edges.

The derivation assumes that the charges of ions are independent. This assumption is valid for electrolyte solutions in the grand canonical ensemble, where electroneutrality needs only to be satisfied on average.[59] There is, however, a weak dependence between the charges of different ions in the canonical ensemble since there must always be an equal number of anions and cations to satisfy electroneutrality. Equivalence of ensembles[59] suggests that the statistics of both ensembles should converge in the thermodynamic limit.

APPENDIX E: LATTICE GAS MODEL FOR NITROGEN

How the simulation procedure described in Sec. III was adjusted to fit the modeling of a dilute nitrogen gas at 5 bar and 25 °C?

At low densities, the Lennard-Jones model accounts correctly for both repulsion and dispersion forces observed between polarizable neutral atoms.[60] According to this model, molecules i and j interact according to the potential

$$u_{ij} = 4\varepsilon_{\mathrm{LJ}}\left[\left(\frac{\sigma_{\mathrm{LJ}}}{r_{ij}}\right)^{12} - \left(\frac{\sigma_{\mathrm{LJ}}}{r_{ij}}\right)^{6}\right]. \tag{E1}$$

Here, σ_{LJ} and $-\varepsilon_{\mathrm{LJ}}$ are the collision diameter and minimum value of the potential, respectively. The Lennard-Jones model is similar to the lattice gas defined by the potential[61]

$$u_{ij} = -4\varepsilon_{\mathrm{LJ}}\left(\frac{\sigma_{\mathrm{LJ}}}{r_{ij}}\right)^{6}, \tag{E2}$$

to the extent that the lattice gas mimics the repulsive forces indirectly by excluding microstates with overlapping molecules. Such a lattice gas can be implemented using the same procedure as in Sec. III,

but with a lattice spacing equal to σ_{LJ} as a measure of the minimum approach distance between ions. This procedure is equivalent to modelling nitrogen as a non-Coulomb lattice gas.

The Results and Discussion section shows the EMD of a non-Coulomb lattice gas corresponding to nitrogen gas at approximately the density of an ideal gas at 5 bar and 25 °C. This system was simulated by naively sampling 10^5 microstates of a system with $N_m = 300$ molecules in a box of length $36\sigma_{LJ}$, which corresponds to a reduced density $\rho\sigma_{LJ}^3 = 6.430 \times 10^{-3}$. The simulated system corresponds approximately to the density at the previously mentioned temperature and pressure, where the reduced density and reduced β of nitrogen gas, respectively, are

$$\rho\sigma_{LJ}^3 = 6.334 \times 10^{-3} \tag{E3}$$

and

$$\beta\varepsilon_{LJ} = 0.320. \tag{E4}$$

Equations (E3) and (E4) are consistent with the density of an ideal gas when using Edalat's[62] estimate for σ_{LJ} and ε_{LJ} of nitrogen, namely,

$$\sigma_{LJ} = 3.736 \times 10^{-10}\ \text{m} \tag{E5}$$

and

$$\varepsilon_{LJ}/k_B = 95.48\ \text{K}. \tag{E6}$$

REFERENCES

[1] P. Debye and E. Hückel, "Zur theorie der elektrolyte. I. Gefrierpunktserniedrigung und verwandte erscheinungen," Phys. Z. **24**, 185–206 (1923).

[2] F. F. Chen, *Introduction to Plasma Physics and Controlled Fusion*, 3rd ed. (Springer International Publishing AG, Cham, Switzerland, 2016), Sec. 1, pp. 8–11.

[3] K. B. Oldham, *Electrochemical Science and Technology: Fundamentals and Applications*, 1st ed. (John Wiley & Sons, Chichester, England, 2012), Sec. 2, pp. 41–45.

[4] M. L. Michelsen and J. M. Mollerup, *Thermodynamic Models: Fundamentals & Computational Aspects*, 2nd ed. (Tie-Line Publications, Holte, Denmark, 2007), Sec. 6.4, pp. 176–184.

[5] D. A. McQuarrie, *Statistical Mechanics*, 1st ed. (Harper & Row, New York, 1976), Sec. 15.1, pp. 326–340.

[6] Y. Levin, "Introduction to statistical mechanics of charged systems," Braz. J. Phys. **34**, 1158–1176 (2004).

[7] R. H. Fowler and E. A. Guggenheim, *Statistical Thermodynamics*, 2nd ed. (Cambridge University Press, Cambridge, UK, 1956), Sec. 9, pp. 377–420.

[8] L. Ellingsen, "An investigation of the thermodynamic and dielectric properties of primitive and non-primitive electrolyte models in the limit of infinite dilution using a simplest possible first-principle approach," M.S. thesis, Norwegian University of Science and Technology, Department of Chemistry, 2020.

[9] G. M. Silva, X. Liang, and G. M. Kontogeorgis, "On the derivations of the Debye–Hückel equations," Mol. Phys. **120**, e2064353 (2022).

[10] H. S. Frank and P. T. Thompson, "Fluctuations and the limit of validity of the Debye–Hückel theory," J. Chem. Phys. **31**, 1086–1095 (1959).

[11] T. S. Sørensen, "How wrong is the Debye–Hückel approximation for dilute primitive model electrolytes with moderate bjerrum parameter?," J. Chem. Soc., Faraday Trans. **86**, 1815–1843 (1990).

[12] T. S. Sørensen, P. Sloth, H. B. Nielsen, and J. B. Jensen, "On the validity of the Debye–Hückel laws for dilute electrolyte solutions tested by high-precision Monte Carlo simulations. Towards a rational thermodynamics. V," Acta Chem. Scand., Ser. A **42**, 237–253 (1988).

[13] G. M. Kontogeorgis, B. Maribo-Mogensen, and K. Thomsen, "The Debye-Hückel theory and its importance in modeling electrolyte solutions," Fluid Phase Equilib. **462**, 130–152 (2018).

[14] J.-P. Simonin, "On the 'Born' term used in thermodynamic models for electrolytes," J. Chem. Phys. **150**, 244503 (2019).

[15] I. Y. Shilov and A. K. Lyashchenko, "The role of concentration dependent static permittivity of electrolyte solutions in the Debye–Hückel theory," J. Phys. Chem. B **119**, 10087–10095 (2015).

[16] I. Y. Shilov and A. K. Lyashchenko, "Modeling activity coefficients in alkali iodide aqueous solutions using the extended Debye–Hückel theory," J. Mol. Liq. **240**, 172–178 (2017).

[17] I. Y. Shilov and A. K. Lyashchenko, "Comment on 'The Debye–Hückel theory and its importance in modeling electrolyte solutions,'" Fluid Phase Equilib. **485**, 248–250 (2019).

[18] I. Y. Shilov and A. K. Lyashchenko, "Anion-specific effects on activity coefficients in aqueous solutions of sodium salts: Modeling with the extended Debye–Hückel theory," J. Solution Chem. **48**, 234–247 (2019).

[19] L. Sun, Q. Lei, B. Peng, G. M. Kontogeorgis, and X. Liang, "An analysis of the parameters in the Debye-Hückel theory," Fluid Phase Equilib. **556**, 113398 (2022).

[20] L. Sun, X. Liang, N. v. Solms, and G. M. Kontogeorgis, "Analysis of some electrolyte models including their ability to predict the activity coefficients of individual ions," Ind. Eng. Chem. Res. **59**, 11790–11809 (2020).

[21] Q. Lei, B. Peng, L. Sun, J. Luo, Y. Chen, G. M. Kontogeorgis, and X. Liang, "Predicting activity coefficients with the Debye–Hückel theory using concentration dependent static permittivity," AIChE J. **66**, 16651 (2020).

[22] F. Malatesta, A. Giacomelli, and R. Zamboni, "Activity coefficients of electrolytes from the EMF of liquid membrane cells. III: $LaCl_3$, $K_3Fe(CN)_6$, and $LaFe(CN)_6$," J. Solution Chem. **23**, 11–36 (1994).

[23] D. Fraenkel, "Negative deviations from the Debye–Hückel limiting law for high-charge polyvalent electrolytes: Are they real?," J. Chem. Theory Comput. **14**, 2609–2620 (2018).

[24] T. Biver and F. Malatesta, "Comment on 'negative deviations from the Debye–Hückel limiting law for high-charge polyvalent electrolytes: Are they real?,'" J. Chem. Theory Comput. **14**, 6427–6433 (2018).

[25] D. Fraenkel, "Reply to 'Comment on 'negative deviations from the Debye–Hückel limiting law for high-charge polyvalent electrolytes: Are they real?','" J. Chem. Theory Comput. **14**, 6434–6442 (2018).

[26] S. R. Milner, "XLIX. The virial of a mixture of ions," London, Edinburgh Dublin Philos. Mag. J. Sci. **23**, 551–578 (1912).

[27] S. R. Milner, "LXXIX. The effect of interionic forces on the osmotic pressure of electrolytes," London, Edinburgh Dublin Philos. Mag. J. Sci. **25**, 742–751 (1913).

[28] C. L. Perrin, I. Agranat, A. Bagno, S. E. Braslavsky, P. A. Fernandes, J.-F. Gal, G. C. Lloyd-Jones, H. Mayr, J. R. Murdoch, N. S. Nudelman, L. Radom, Z. Rappoport, M.-F. Ruasse, H.-U. Siehl, Y. Takeuchi, T. T. Tidwell, E. Uggerud, and I. H. Williams, "Glossary of terms used in physical organic chemistry (IUPAC recommendations 2021)," Pure Appl. Chem. **94**, 353–534 (2022).

[29] S. Friedli and Y. Velenik, *Statistical Mechanics of Lattice Systems: A Concrete Mathematical Introduction*, 1st ed. (Cambridge University Press, Cambridge, UK, 2017), Sec. 6, pp. 262–345.

[30] A. B. Walker and M. J. Gillan, "Thermodynamics of the Coulomb lattice gas," Solid State Phys. **16**, 3025–3044 (1983).

[31] A. Diehl and A. Z. Panagiotopoulos, "Phase diagrams in the lattice restricted primitive model: From order-disorder to gas-liquid phase transition," Phys. Rev. E **71**, 046118 (2005).

[32] A. Z. Panagiotopoulos and S. K. Kumar, "Large lattice discretization effects on the phase coexistence of ionic fluids," Phys. Rev. Lett. **83**, 2981–2984 (1999).

[33] L. Mitáš, "Thermodynamics of the Coulomb lattice gas within the mean spherical approximation," Solid State Commun. **65**, 1401–1404 (1988).

[34] A. R. Leach, *Molecular Modelling: Principles and Applications*, 2nd ed. (Pearson Education, Harlow, England, 2001), Sec. 6.7, pp. 324–334.

[35] A. C. F. Ribeiro, M. A. Esteso, V. M. M. Lobo, H. D. Burrows, A. M. Amado, A. M. Amorim da Costa, A. J. F. N. Sobral, E. F. G. Azevedo, and M. A. F. Ribeiro,

"Mean distance of closest approach of ions: Sodium salts in aqueous solutions," J. Mol. Liq. **128**, 134–139 (2006).
[36]J. Kielland, "Individual activity coefficients of ions in aqueous solutions," J. Am. Chem. Soc. **59**, 1675–1678 (1937).
[37]*CRC Handbook of Chemistry and Physics*, edited by W. M. Haynes, 95th ed. (CRC Press/Taylor & Francis, Boca Raton, FL, 2014).
[38]C. G. Malmberg and A. A. Maryott, "Dielectric constant of water from 0° to 100 °C," J. Res. Natl. Inst. Stand. Technol. **56**, 1–8 (1956).
[39]E. Waisman and J. L. Lebowitz, "Mean spherical model integral equation for charged hard spheres I. Method of solution," J. Chem. Phys. **56**, 3086–3093 (1972).
[40]M. P. Allen and D. J. Tildesley, *Computer Simulation of Liquids*, 2nd ed. (Oxford University, Oxford, UK, 2017), Sec. 4, pp. 147–160.
[41]D. Frenkel, *Understanding Molecular Simulation: From Algorithms to Applications*, 2nd ed. (Academic Press, San Diego, CA, 2002), Sec. 3, pp. 23–62.
[42]R. Durstenfeld, "Algorithm 235: Random permutation," Commun. ACM **7**, 420 (1964).
[43]M. Eberl, *Fisher–Yates Shuffle* (Archive Formal Proofs, 2016).
[44]D. W. Scott, "On optimal and data-based histograms," Biometrika **66**, 605–610 (1979).
[45]D. W. Scott, "Histogram," Wiley Interdisp. Rev.: Comput. Stat. **2**, 44–48 (2010).
[46]N. Metropolis, A. W. Rosenbluth, M. N. Rosenbluth, A. H. Teller, and E. Teller, "Equation of state calculations by fast computing machines," J. Chem. Phys. **21**, 1087–1092 (1953).
[47]W. K. Hastings, "Monte Carlo sampling methods using Markov chains and their applications," Biometrika **57**, 97–109 (1970).
[48]D. Gamerman and H. F. Lopes, *Markov Chain Monte Carlo: Stochastic Simulation for Bayesian Inference*, 2nd ed. (Chapman & Hall/CRC, Boca Raton, FL, 2006), Sec. 6, pp. 191–236.
[49]R. de Levie, "When, why, and how to use weighted least squares," J. Chem. Educ. **63**, 10–15 (1986).
[50]T. Strutz, *Data Fitting and Uncertainty: A Practical Introduction to Weighted Least Squares and Beyond*, 1st ed. (Vieweg + Teubner Verlag, Wiesbaden, Germany, 2011).
[51]T. H. Cormen, C. E. Leiserson, R. L. Rivest, and C. Stein, *Introduction to Algorithms*, 3rd ed. (The MIT Press, Cambridge, MA, 2017), Sec. B.4, p. 1172.
[52]T. H. Cormen, C. E. Leiserson, R. L. Rivest, and C. Stein, *Introduction to Algorithms*, 3rd ed. (The MIT Press, Cambridge, MA, 2017), Sec. 23, pp. 624–640.
[53]M. A. Martínez-Fuentes and J. J. E. Herrera-Velázquez, "On the accuracy of the Debye shielding model," Rev. Mex. Fis. E **63**, 63–67 (2017).
[54]G. Livadiotis and D. J. McComas, "Electrostatic shielding in plasmas and the physical meaning of the Debye length," J. Plasma Phys. **80**, 341–378 (2014).
[55]C. Robert and L. A. Shepp, "On the sum of symmetric random variables," Am. Stat. **37**, 237 (1983).
[56]F. A. Kassan-ogly, "One-dimensional Ising model with next-nearest-neighbour interaction in magnetic field," Phase Transitions **74**, 353–365 (2001).
[57]F. Taherkhani, E. Daryaei, H. Abroshan, H. Akbarzadeh, G. Parsafar, and A. Fortunelli, "On the existence of an analytic solution to the 1-d Ising model with nearest and next-nearest neighbor interactions in the presence of a magnetic field," Phase Transitions **84**, 77–84 (2011).
[58]C. Z. Mooney and R. D. Duval, *Bootstrapping: A Nonparametric Approach to Statistical Inference*, 1st ed., Quantitative Applications in the Social Sciences Vol. 95 (SAGE Publications, Inc, Newbury Park, CA, 1993).
[59]V. B. Bobrov, I. M. Sokolov, and S. A. Trigger, "Necessary conditions of the equivalence of canonical and grand canonical ensembles in Coulomb system thermodynamics," Phys. Plasmas **19**, 062101 (2012).
[60]J. N. Israelachvili, *Intermolecular and Surface Forces*, 2nd ed. (Academic Press Limited, London, UK, 1991), Secs. 6–7, pp. 83–121.
[61]A. Campa, T. Dauxois, and S. Ruffo, "Statistical mechanics and dynamics of solvable models with long-range interactions," Phys. Rep. **480**, 57–159 (2009).
[62]M. Edalat, "Optimized parameters and exponents of Mie (n,m) intermolecular potential energy function based on the shape of molecules," Int. J. Thermophys. **1**, 177–184 (1980).